

Article

Phosphorus/Sulfur-Enriched Reduced Graphene Oxide Papers Obtained from Recycled Graphite: Solid-State NMR Characterization and Electrochemical Performance for Energy Storage

Mariana A. Vieira ^{1,*}, Tainara L. G. Costa ¹, Gustavo R. Gonçalves ¹, Daniel F. Cipriano ¹, Miguel A. Schettino, Jr. ¹, Elen L. da Silva ², Andrés Cuña ² and Jair C. C. Freitas ^{1,*}

¹ Laboratory of Carbon and Ceramic Materials, Department of Physics, Federal University of Espírito Santo, Vitória 29075-910, Brazil; guerratainara@gmail.com (T.L.G.C.); gustavo.rgoncalves@hotmail.com (G.R.G.); danielcipriano.fisica@gmail.com (D.F.C.); miguel.ufes@gmail.com (M.A.S.J.)

² Área Físicoquímica, DETEMA, Facultad de Química, Universidad de la República, CC 1157, Montevideo 11800, Uruguay; elenlealdasilva@gmail.com (E.L.d.S.); acunasuarez@gmail.com (A.C.)

* Correspondence: m.arpinivieira@gmail.com (M.A.V.); jairccfreitas@yahoo.com.br (J.C.C.F.)

Abstract: The reduction of graphene oxide (GO) by means of thermal and/or chemical treatments leads to the production of reduced graphene oxide (rGO)—a material with improved electrical conductivity and considered a viable and low-cost alternative to pure graphene in several applications, including the production of supercapacitor electrodes. In the present work, GO was prepared by the oxidation of graphite recycled from spent Li-ion batteries using mixtures of sulfuric and phosphoric acids (with different H₂SO₄/H₃PO₄ ratios), leading to the production of materials with significant S and P contents. These materials were then thermally reduced, resulting in rGO papers that were investigated by solid-state ¹³C and ³¹P nuclear magnetic resonance, along with other methods. The electrochemical properties of the produced rGO papers were evaluated, including the recording of cyclic voltammetry and galvanostatic charge–discharge curves, besides electrochemical impedance spectroscopy analyses. The samples obtained by thermal reduction at 150 °C exhibited good rate capability at high current density and high capacitance retention after a large number of charge–discharge cycles. The results evidenced a strong relationship between the electrochemical properties of the produced materials and their chemical and structural features, especially for the samples containing both S and P elements. The methods described in this work represent, then, a facile and low-cost alternative for the production of rGO papers using graphite recycled from spent batteries, with promising applications as supercapacitor electrodes.

Keywords: graphene oxide; reduced graphene oxide; solid-state NMR; electrochemical properties



Citation: Vieira, M.A.; Costa, T.L.G.; Gonçalves, G.R.; Cipriano, D.F.; Schettino, M.A., Jr.; da Silva, E.L.; Cuña, A.; Freitas, J.C.C. Phosphorus/Sulfur-Enriched Reduced Graphene Oxide Papers Obtained from Recycled Graphite: Solid-State NMR Characterization and Electrochemical Performance for Energy Storage. *C* **2023**, *9*, 60. <https://doi.org/10.3390/c9020060>

Academic Editors: Olena Okhay and Gil Gonçalves

Received: 1 May 2023

Revised: 6 June 2023

Accepted: 8 June 2023

Published: 12 June 2023



Copyright: © 2023 by the authors. Licensee MDPI, Basel, Switzerland. This article is an open access article distributed under the terms and conditions of the Creative Commons Attribution (CC BY) license (<https://creativecommons.org/licenses/by/4.0/>).

1. Introduction

Since 2004, when Novoselov et al. [1] reported a method for obtaining graphene layers by mechanical exfoliation of graphite, the search for alternative routes to produce graphene-based materials has grown remarkably. The oxidation of graphite to produce graphite oxide, first reported almost 160 years ago [2], has attracted considerable interest as a potential method for the low-cost and mass production of graphene-based materials [3,4]. Graphite oxide has a structure somewhat similar to graphite, but containing oxygenated functions such as hydroxyls, epoxides, carboxylic acids, ketones, and esters linked to its basal planes, which allows the intercalation of water molecules between them, causing a significant increase in the interlayer spacing. As a result, these layers can be easily exfoliated in water, giving rise to a material made up of single layers (or groups of a few stacked layers) called graphene oxide (GO) [5,6]. GO can then be reduced to form sheets similar to graphene by removing oxygenated functions and recovering most of the

sp^2 bonds in the basal planes, leading to the formation of a material known as reduced graphene oxide (rGO) which exhibits good electrical conductivity and, despite the presence of structural defects and chemical heterogeneity, can be a viable, low-cost alternative to pristine graphene in several applications [6]. The reduction of GO can be accomplished through various approaches, such as chemical reduction with hydrazine [7,8], hydrogen plasma [9], pulsed laser irradiation [10], gamma ray irradiation [11], and thermal treatments [12,13]. Different reduction methods lead to the production of rGO samples with different degrees of reduction which may therefore contain some remaining oxygen functionalities, directly affecting the properties and performance of the material depending on the area in which it is to be applied. Some methods, such as reduction with hydrazine and thermal treatments, can also be used together to obtain samples of rGO with a minimum content of oxygenated functions and with maximum restoration of the sp^2 layers (and, consequently, of the electrical conductivity) [7,14]. In cases where there is no need for a high degree of structural order or excellent electrical conductivity, thermal annealing at low temperatures (typically 90 to 300 °C) represents a simple and low-cost approach for GO reduction, allowing the obtention of rGO samples with good properties for applications in gas sensing or electrochemical devices [12,15].

Graphene-based materials obtained by liquid-phase exfoliation, such as GO and rGO, offer the possibility of changing the chemical and surface properties through the insertion of heteroatoms and/or functional groups, which can also contribute to many sensing and electrochemical device applications [16]. For instance, the methods used in most previous studies for the preparation of P-functionalized GO or rGO-based materials involve reactions conducted at several steps and using varied phosphorus sources such as phytic acid [17], diammonium hydrogen phosphate [18], red phosphorus [18], phosphorus trichloride [19], triphenylphosphine [20] and phosphoric acid [21]. A substantial simplification of the process of the incorporation of phosphorus into the structure of GO and rGO can be achieved by using H_3PO_4 directly in the reaction of graphite oxidation. In fact, the so-called Marcano–Tour method [22] involves a modification of the original graphite oxidation method proposed by Hummers and Offeman [23], replacing H_2SO_4 with a 9:1 (*v/v* ratio) H_2SO_4/H_3PO_4 mixture. Previous reports have shown that GO samples prepared by the Marcano–Tour method exhibit a high degree of oxidation, resulting in general in O/C atomic ratios larger than those reached by using the Hummers method [22–25].

In this work, an investigation was conducted aiming to better understand the nature of the S- and P-containing groups present in GO samples prepared from the oxidation of graphite in acid mixtures with varied H_2SO_4/H_3PO_4 proportions and in rGO samples produced by subsequent thermal treatments; solid-state ^{13}C and ^{31}P nuclear magnetic resonance (NMR), Fourier-transform infrared spectroscopy (FTIR), and X-ray diffraction (XRD) were the main tools used to probe the chemical and structural features of the GO and rGO samples. Finally, the electrochemical behavior of the rGO samples was investigated, showing an intimate connection between the electrochemical performance of the produced materials and their chemical and structural features which were defined by the conditions used in the GO synthesis.

2. Experimental Methods

2.1. Samples Preparation

Materials

The precursor used for the production of GO was recycled graphite derived from spent lithium-ion batteries, as reported elsewhere [25]. The graphite present in the anode of the spent batteries was separated from the copper foil by dissolution in concentrated HNO_3 , followed by filtration, washing with abundant distilled water and drying at 100 °C for 3 h. The other reactants were $KMnO_4$, H_3PO_4 (85%) and H_2SO_4 (95%) from Vetec (Duque de Caxias, Brazil), $NaNO_3$ and H_2O_2 (30 vol.%) from Cromoline (Diadema, Brazil).

Preparation of phosphorus and sulfur-containing graphene oxide (P/S-GO) and reduced graphene oxide papers (P/S-rGO):

The P/S-GO samples were prepared using the Marcano–Tour method [22], varying the ratio of $\text{H}_2\text{SO}_4/\text{H}_3\text{PO}_4$ used. For the conventional Marcano–Tour method, 1 g of graphite, 6 g of KMnO_4 , and 135 mL of a 9:1 (*v/v* ratio) $\text{H}_2\text{SO}_4/\text{H}_3\text{PO}_4$ solution were mixed. The mixture was kept in a water bath at 50 °C and stirred for 12 h. After this time, the mixture was poured into 400 mL of crushed ice, and 3 mL of a 30% *v/v* H_2O_2 were added, leading to a change in the color of the mixture from dark brown to intense yellow. The mixture was allowed to stand for 24 h to decant the product. To remove the excess acid, the precipitate was washed with distilled water and centrifuged until the supernatant reached a pH between 5 and 6. In order to obtain the GO samples with varying P and S contents, reactions were also performed using 1:1 and 1:2 (*v/v* ratios) $\text{H}_2\text{SO}_4/\text{H}_3\text{PO}_4$ solutions, following the same protocol as in the conventional method. The GO samples containing P and S (generally named P/S-GO samples) were then dried at 80 °C and were called GOT x , in which x indicates the $\text{H}_2\text{SO}_4/\text{H}_3\text{PO}_4$ ratio: $x = 91, 11, \text{ or } 12$ for 9:1, 1:1, and 1:2 *v/v* ratios, respectively.

After preliminary studies (as stated in the Supplementary Information), samples of thermally reduced graphene oxide paper were produced by the thermal treatment of the GO samples that were synthesized in the previous step. The P/S-GO suspensions obtained at the end of each reaction and washing process were divided into 2 mL aliquots, which were directly submitted to two different treatments in a lab oven, under ambient atmosphere, using two treatment temperatures (100 and 150 °C) for 24 h. At the end of the process, rGO papers were obtained, and these samples were named GOT x_n , where x indicates the $\text{H}_2\text{SO}_4/\text{H}_3\text{PO}_4$ volume ratio used in the synthesis (as described above) and n indicates the heat treatment temperature (100 or 150 °C).

2.2. Characterization

2.2.1. X-ray Diffraction (XRD)

The X-ray diffractograms of the precursor graphite, GO and rGO papers were recorded on a Shimadzu (Columbia, MD, USA) XRD-6000 diffractometer. The samples were ground and the experiments were conducted at room temperature using $\text{Cu-K}\alpha$ radiation ($\lambda = 1.5418 \text{ \AA}$) and with the angle of diffraction (2θ) varying from 5 to 50° in steps of 0.04°.

2.2.2. Solid-State ^{13}C and ^{31}P NMR

Solid-state NMR experiments were performed at room temperature on a Varian/Agilent (Palo Alto, CA, USA) commercial spectrometer operating in a 9.4 T magnetic field, which corresponds to a frequency of 100.5 MHz for ^{13}C and 161.8 MHz for ^{31}P . Magic angle spinning (MAS) at 14 kHz was employed in all experiments, with the powdered samples packed into a 4 mm diameter zirconia rotor. The ^{13}C NMR experiments were conducted using a pulse sequence specially designed to avoid background signals from contributions external to the probe (which are common in ^{13}C NMR spectra obtained by direct excitation of the ^{13}C nuclei), with a $\pi/2$ pulse (4.3 μs) immediately followed by a pair of π pulses (8.6 μs) and subsequent detection of the free induction decay (FID) [26]. In all the ^{13}C NMR experiments, the recycle delay was 15 s and the spectral width was 250 kHz. All spectra were obtained by the Fourier transform of the FID after the accumulation of ca. 4000 transients. The ^{13}C chemical shifts were referenced to tetramethylsilane (TMS) using hexamethylbenzene as a secondary reference. The ^{31}P NMR experiments were conducted using single-pulse excitation (SPE) with a $\pi/2$ pulse with duration of 4.0 μs and a recycle delay of 60 s. The spectra were obtained by the Fourier transform of the FID after the accumulation of ca. 500 transients, and the chemical shifts were referenced to an 85 wt.% aqueous H_3PO_4 solution using $\text{NH}_4\text{H}_2\text{PO}_4$ ($\delta = 0.9 \text{ ppm}$) as a secondary reference.

2.2.3. Fourier-Transform Infrared (FTIR) Spectroscopy

The infrared absorption spectroscopy analyses were conducted directly using pulverized GO and rGO samples on a Spectrum 100 (Perkin Elmer, Waltham, MA, USA) spectrometer in transmittance mode, equipped with an attenuated total reflection (ATR)

attachment with a diamond crystal. The spectra were acquired using 64 scans and a 2 cm^{-1} resolution. The pulverized samples were directly deposited on the top of the ATR crystal, without the need of any additional sample preparation steps.

2.2.4. X-ray Fluorescence (XRF)

The XRF analyses to determine the P and S contents of the GO and rGO samples were performed on an EDX700 (Shimadzu, (Columbia, MD, USA) spectrometer equipped with a Rhodium (Rh) X-ray tube. This instrument operated at 15 kV, with collimation of 10 mm of the incident beam for 4 min per sample. The Sodium–Scandium (Na–Sc) energy channel was used and the analyzed energy interval was from 0.00 to 20.48 keV, with a scanning step of 0.01 keV. To minimize matrix effects and enhance the accuracy of the quantification, a carbonaceous sample with negligible P and S contents was selected as the matrix for the construction of the calibration curves. The calibration curves for phosphorus (P) and sulfur (S) were constructed by adding known concentrations of $\text{NH}_4\text{H}_2\text{PO}_4$ (corresponding to P contents of 0.1, 0.5, 1.0, 2.0, 3.0, and 5.0 wt.%) and Na_2SO_4 (corresponding to S contents of 1.0, 5.0, 10.0, 15.0 and 20.0 wt.%), respectively, to the carbon powder (with a mass of ca. 1 g). The intensities of the XRF lines corresponding to P and S were recorded for each calibration sample. The calibration curves were obtained through linear regression; high values of the coefficients of determination (~ 0.99) were obtained in the full range of P and S contents used to construct the calibration curves, allowing the determination of the P contents between 0.1 and 5.0 wt.% and of S contents between 1.0 and 20.0 wt.%. To ensure representative sampling and homogeneity, the samples were pulverized and sieved prior to the analyses. GO and rGO samples with approximately 300 mg were consistently used for all XRF measurements. The samples were submitted to the analyses without any additional treatment or manipulation, and 3–5 independent analyses were performed for each sample. The standard deviations obtained from these measurements were assumed to represent the uncertainties of the average values.

2.2.5. Electrochemical Characterization

For the electrochemical analysis, a symmetric two-electrode Swagelok[®] (Buenos Aires, Argentina)-type cell with two tantalum rods as current collectors was used. The cell electrodes were prepared by cutting an rGO paper (GO treated at $150\text{ }^\circ\text{C}$ for 24 h) sample as a rectangular electrode with a cross-section area of 0.32 cm^2 and weighing ca. 1.0 mg (Figure 1). A sulfuric acid aqueous solution (2 mol L^{-1}) was used as the electrolyte, and a glassy microfibre paper (Whatman 934 AH—Maidstone, UK) was chosen as the electrode separator. Electrochemical characterization included the recording of galvanostatic charge–discharge curves (in a current density range of $1\text{--}8\text{ A g}^{-1}$), cyclic voltammograms (at 5, 10, 20 and 50 mV s^{-1}) obtained in a voltage range of $0\text{--}1\text{ V}$, and electrochemical impedance spectroscopy (EIS) measurement in the frequency range of $5.0 \times 10^{-4}\text{--}2.5 \times 10^5\text{ Hz}$. The gravimetric specific capacitance (C_s) was determined from galvanostatic charge–discharge measurements at each current according to equation

$$C_s = 2 \cdot I \cdot t_d / E_2 \cdot m_e \quad (1)$$

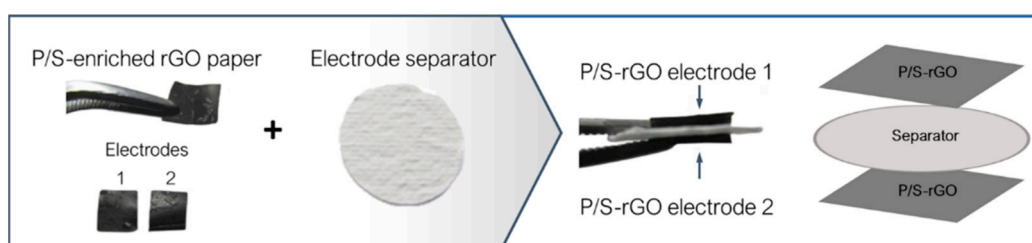


Figure 1. Schematic diagram showing the assembly of the laboratory supercapacitor for electrochemical analyses.

In this expression, I is the applied current, t_d is the discharge time, E_2 is the voltage range during the discharge and m_e is the mass of one electrode. All measurements were carried out at room temperature using a potentiostat/galvanostat/FRA Vertex (Ivium Technologies, De Lismortel, Netherlands).

3. Results and Discussion

A preliminary study (described in the Supplementary Information section) showed that the thermal treatment of a GO sample—subjecting it to the temperature of 150 °C for 24 h in a lab oven—proved to be efficient for obtaining an rGO paper with few remaining oxygen functionalities (mostly carboxylic acids, as verified by solid-state ^{13}C NMR spectroscopy). Based on that, the GO suspension obtained at the end of each reaction of the employed Marcano–Tour method [22] (using three $\text{H}_2\text{SO}_4/\text{H}_3\text{PO}_4$ mixtures at 9:1, 1:1 and 1:2 v/v ratios) was submitted to two different thermal treatments in the same lab oven at ambient atmosphere and at temperatures of 100 and 150 °C for 24 h, which provided several P/S-GO and P/S-rGO samples in the form of papers [27], with thicknesses ranging from ca. 10 to 20 μm as estimated by scanning electron microscopy (SEM); details are provided in the Supplementary Information section (Figure S7).

The sulfur and phosphorus contents of the P/S-GO and P/S-rGO papers were evaluated by XRF analysis; the results (given in Table 1) confirmed that by changing the $\text{H}_2\text{SO}_4/\text{H}_3\text{PO}_4$ ratio, one can vary the S and P contents in the synthesized GO samples, with S contents varying from 1.1 to 3.6 wt.% (GOT11 and GOT91, respectively), and P contents varying from 0.26 to 2.8 wt.% (for GOT91 and GOT12, respectively). It is worth noting that these S contents are somewhat inferior to the value corresponding to a similar GO sample prepared by a modified Hummers method (with no addition of H_3PO_4), as described in the Supplementary Information section (Table S2). The thermal treatment at 150 °C did not cause the complete removal of whatever S and P functionalities present in the synthesized GO samples; thus, the method presented here can be considered effective for the production S- and P-containing rGO samples, with S contents varying from 2.1 to 6.8 wt.% (GOT12_150 and GOT91_150, respectively), and P contents varying from 0.27 to 5.4 wt.% (for GOT91_150 and GOT12_150, respectively). Given that most synthetic approaches involve the use of concentrated sulfuric acid, such as the methods of Hummers [23] and Marcano–Tour [22], the presence of sulfur in GO can be expected. Previous elemental analysis results showed that the concentration of S can reach 6 wt.% depending on the chosen synthetic method, and this concentration occurs predominantly due to the presence of organosulfate-type groups [28]. Due to their low hydrolysis rate, these sulfonated groups tend to remain in the GO structure even after a thorough washing and, although often disregarded, these S concentrations can directly affect the GO properties [6,29]. Similarly, phosphorus can also be present in low concentrations in GO (<0.1 wt.%), especially in samples prepared by methods that follow the Marcano–Tour route [22], in which the oxidation reaction takes place in the presence of concentrated phosphoric acid. The hydrolysis of phosphorus functionalities also occurs slowly, and therefore phosphate derivatives are expected to occur in the structure of the GO samples synthesized in the presence of H_3PO_4 [22,25,30].

Table 1. XRF results for P and S contents of the P/S-GO samples synthesized by the Marcano–Tour method and the corresponding reduced samples.

Sample	P Content (wt.%)	S Content (wt.%)
GOT91	0.26 ± 0.01	3.6 ± 0.2
GOT91_150	0.27 ± 0.01	6.8 ± 0.3
GOT11	1.4 ± 0.1	1.1 ± 0.1
GOT11_150	2.3 ± 0.1	2.7 ± 0.1
GOT12	2.8 ± 0.1	1.4 ± 0.1
GOT12_150	5.4 ± 0.3	2.1 ± 0.1

The XRD results (Figure 2) of the synthesized GOs clearly demonstrated the efficiency of the reactions following both conventional and modified Marciano–Tour methods [22], indicating the formation of the structure expected for GOs by the appearance of an intense diffraction peak at $2\theta \cong 8\text{--}10^\circ$ for all samples [31,32]. It is possible to note that treating samples at 100°C did not cause significant changes in any of the corresponding XRD patterns. A small displacement of the main diffraction peak from $2\theta \cong 8\text{--}10^\circ$ to higher angles was observed in the case of the samples thermally treated at 100°C when compared to the case of the XRD patterns of the GO parent materials. In addition, a broadening of this peak and an attenuation of its intensity were observed, accompanied by the appearance of a broad peak at $2\theta \cong 18\text{--}22^\circ$; this new diffraction peak indicated the formation of a new phase with a drastic decrease in its interlayer spacing to ca. 4 \AA , which is a value much smaller than the corresponding interlayer spacing of 9 \AA found for the GO samples (GOT91, GOT11 and GOT12). The coexistence of these two peaks shows that the reduction process is not abrupt (i.e., there are regions with intermediate interplanar spacing formed during the thermal reduction) and does not happen at the same time throughout the whole sample, in agreement with previous reports [12,15,33].

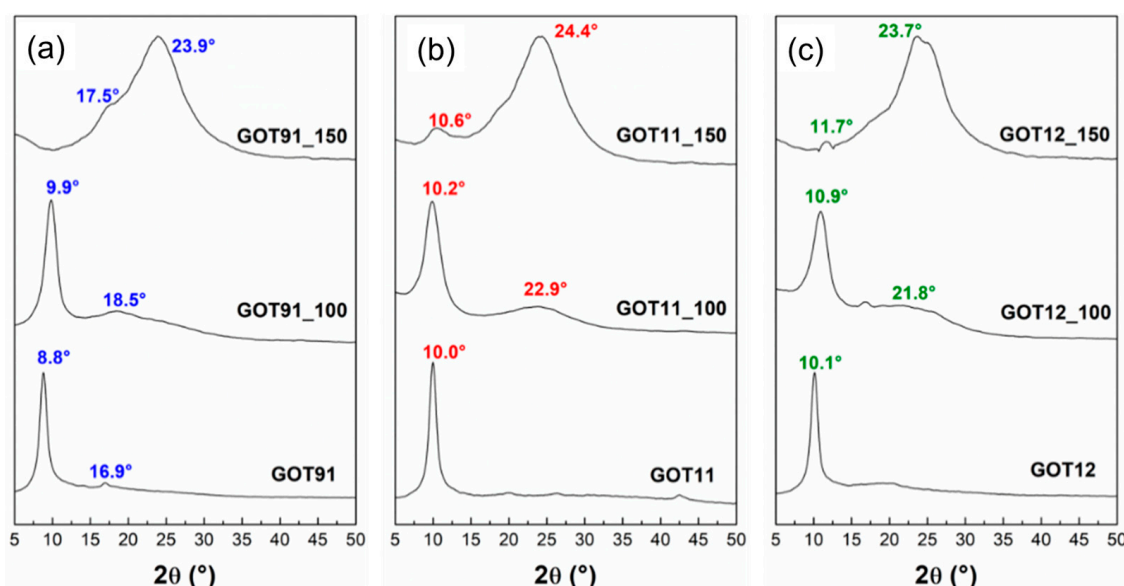


Figure 2. X-ray diffractograms of the (a) GOT91, (b) GOT11 and (c) GOT12 samples as prepared and after the thermal reduction treatments performed at 100 and 150°C .

On the other hand, for samples treated at 150°C , it is possible to notice in the X-ray diffractograms of all P/S-rGO samples that the peak near $2\theta \cong 8\text{--}10^\circ$ (for the original GO samples) is almost completely eliminated. In addition, the presence of a broad and intense diffraction peak at $2\theta \cong 24^\circ$ indicates the formation of a turbostratic-like structure; in this arrangement, the basal planes are stacked in an approximately parallel way, with some degree of curvature and defects, but randomly oriented in relation to each other, with an interlayer spacing ($\sim 3.7\text{ \AA}$) somewhat larger than the value corresponding to graphite (3.35 \AA) [5,33]. Nevertheless, the XRD patterns of all samples treated at 150°C still exhibit broad and low-intensity peaks at lower angles, indicating the presence of a phase with nanostructured arrangement of defective graphene planes and possibly still containing residues of oxygenated functional groups [12,34]. Therefore, the samples thermally reduced for 24 h at 150°C have characteristics compatible with those of the material known as reduced graphene oxide [12,34].

The solid-state ^{13}C NMR results (Figure 3) confirm the successful synthesis of GO in all cases, as evidenced by the presence of the typical resonances expected for the GO structure, such as those at $180\text{--}190\text{ ppm}$ (carbonyl groups in ketones), $160\text{--}170\text{ ppm}$ (carbonyl groups in esters or carboxylic acids), 60 ppm (epoxide carbons), 70 ppm (carbons bonded to hydroxyl

groups), 100 ppm (lactol carbons) and 120–140 ppm (aromatic carbons) [25,35,36]. The degree of oxidation of the GOs can be evaluated by ^{13}C NMR by integrating the spectral regions associated with C-OH/C-O-C groups and aromatic sp^2 carbon atoms, indicated as regions A and B, respectively, in Figure 3; the higher the A/B ratio, the higher the degree of oxidation [37,38]. Accordingly, the results shown in Figure 3 demonstrate that the GOT11 sample has an oxidation degree comparable to that of GOT91 (A/B ratios of 2.5 and 2.7, respectively) even after changing the $\text{H}_2\text{SO}_4/\text{H}_3\text{PO}_4$ ratio used in the conventional Marciano–Tour method [22] from 9:1 to 1:1 (*v/v* ratio). However, when the amount of H_3PO_4 is increased even more by changing the acid ratio to 1:2 *v/v*, the GOT12 sample shows a reduced oxidation degree (with an A/B ratio of 1.6), despite the remaining significant presence of oxygenated functionalities and the highest P content (2.8 wt.%) among all as-prepared GO samples analyzed here (see Table 1). The decrease in the size of the basal planes caused by the addition of oxygenated functionalities during the oxidation reaction causes changes in the chemical shift of the peak associated with sp^2 carbons. This occurs due to the reduction in the magnitude of the effects related to the electrical conductivity and diamagnetic susceptibility of the graphene layers, consequently leading to a reduced shielding of the ^{13}C nuclei and, therefore, a higher chemical shift of the peak associated with aromatic sp^2 carbon atoms when compared to the chemical shift of this same peak in non-oxidized graphite samples [37,38]. In light of this information, it is possible to note in the NMR spectra shown in the ^{13}C NMR spectra demonstrated in Figure 3 that the sp^2 carbon peak of the synthesized GOs occurs at slightly different chemical shifts (134 ppm for GOT11 and 129 ppm for GOT12 sample) and has different linewidths depending on the degree of oxidation of each sample. This effect follows the trend predicted by the A/B ratio: GOs with the highest A/B ratios (which indicate a higher degree of oxidation) generally present the highest chemical shifts for the peak associated with aromatic sp^2 carbon atoms.

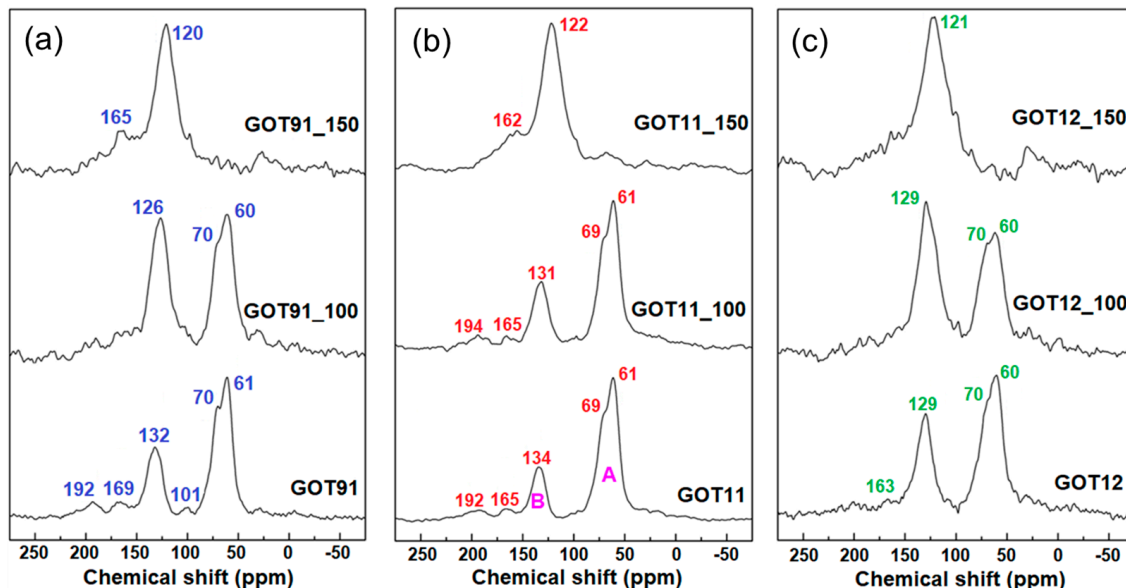


Figure 3. Solid-state ^{13}C NMR spectra of the (a) GOT91, (b) GOT11 and (c) GOT12 samples as prepared and after the thermal reduction treatments performed at 100 and 150 °C.

Analyzing the ^{13}C NMR spectra of the reduced samples, it is possible to note that the peak associated with aromatic sp^2 carbon atoms (chemical shift \cong 130 ppm) is dominant in all samples after the thermal treatment at 150 °C. However, the spectra obtained for samples treated at 100 °C still show significant contribution of the peaks at 60 and 70 ppm, associated with C-O-C and C-OH carbons, respectively [35,38]. Furthermore, the ^{13}C NMR spectra of all thermally treated samples exhibit peaks near 165 and 190 ppm, associated with carbonyl groups; the permanence of groups such as carboxylic acids in these samples

is plausible, since these groups decompose typically above 300 °C [3,15,38]. Another notable aspect in these spectra is the difference in chemical shifts of the peaks relative to aromatic sp^2 carbon atoms. The displacement of these peaks to lower frequencies in the ^{13}C NMR spectra recorded for the thermally treated samples (more notably in the case of the samples treated at 150 °C) is indicative of the reestablishment of the effects related to the electrical conductivity and diamagnetic susceptibility of the graphene layers in the rGO samples [37,38].

The use of solid-state ^{31}P NMR spectroscopy is essential for the characterization of the GO samples synthesized by the conventional and modified Marciano–Tour methods [22] as it allows a detailed understanding of the possible interaction between the GO matrix and phosphorus-containing groups present in the material [25,30]. As previously discussed, GO has a large number of functional groups containing O and H, which are capable of interactions with phosphate groups (with P in a tetrahedral coordination). In solid-state ^{31}P NMR, tetrahedral orthophosphates, in which the central phosphorus atom is pentavalent and bonded to four oxygen atoms, are usually referred to as Q units. The Q units can bridge through the oxygen atoms, forming chains or networks, wherein the amount of bridging oxygen ranges from 0 to 3 depending on the degree of polymerization. In this way, four different Q^n units have been described, where n corresponds to the number of bridging oxygens, that is, of other phosphate groups to which the main unit is linked. The ^{31}P chemical shift associated with such groups is sensitive to the chemical environment of the oxygen atoms directly connected to the phosphorus atom [39–41].

Figure 4 shows the ^{31}P NMR spectra of the GO samples synthesized by conventional and modified Marciano–Tour methods [22]. It is possible to readily observe the differences between the spectra of the three samples, starting with the weak signal-to-noise ratio in the GOT91 spectrum. As all spectra were recorded under similar conditions (including nearly the same number of scans), such difference in signal-to-noise ratio indicates that the P content in the GOT91 sample is considerably lower than that in the GOT11 and GOT12 samples, as confirmed by the XRF results (Table 1). Nevertheless, the detected peak near -9 ppm present in the GOT91 spectrum can be associated with Q^1 units, or pyrophosphoric acid [25,39].

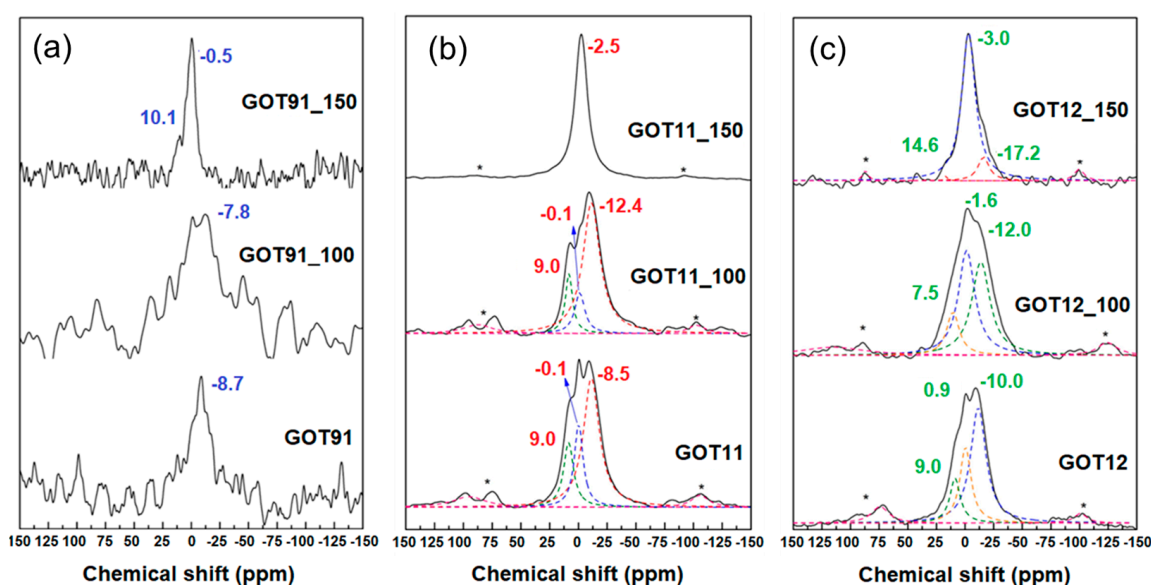


Figure 4. Solid-state ^{31}P NMR spectra of the (a) GOT91, (b) GOT11 and (c) GOT12 samples as prepared and after the thermal reduction treatments performed at 100 and 150 °C. Spinning sidebands are indicated by stars (*).

The ^{31}P NMR spectra of the GOT11 and GOT12 samples show similar profiles, with two peaks centered around 0 and -10 ppm, associated with Q^0 and Q^1 units (or orthophosphoric and pyrophosphoric acids, respectively). The signal intensity in these spectra is higher when compared to that of the spectrum of the GOT91 sample, indicating the increase in the phosphorus content due to the increase in the amount of phosphoric acid used in the synthesis. Thus, through solid-state ^{31}P NMR spectroscopy, it was possible to verify the presence of phosphorus in the samples synthesized by both conventional and modified Marciano–Tour methods [22] using different $\text{H}_2\text{SO}_4/\text{H}_3\text{PO}_4$ volume ratios in a one-step synthesis.

As mentioned above, the peak near -9 ppm present in the ^{31}P NMR spectrum of the GOT91 sample is commonly associated with Q^1 units, or pyrophosphoric acid. After thermally treating this sample at 100°C (GOT91_100), it is possible to detect the presence of a peak of the same nature, probably due to the fact that, at this treatment temperature, the final structure of the product does not differ much from the structure of the conventional sample dried at 80°C (GOT91), as also verified by ^{13}C NMR and XRD. On the other hand, the ^{31}P NMR spectrum of the GOT91_150 sample presents a different behavior, with a peak at -0.5 ppm associated with the presence of orthophosphoric acid (Q^0 units), suggesting a rearrangement of the phosphate groups into isolated H_3PO_4 units, and another peak around 10 ppm, which may be associated with the formation of P-O-C and/or P-C bonds [25,39].

The ^{31}P NMR spectra of the GOT11 and GOT12 samples treated at 100°C exhibit peaks in the region from 7 to 10 ppm, associated with the formation of P-O-C and/or P-C bonds; these bonds are known to occur in reactions in which the amount of phosphorus used is much higher than that of carbon, as used in this work [30,40]. Peaks in the region from -10 to -20 ppm are also detected, which are attributed to the condensation of the phosphate groups leading to the formation of polyphosphoric acids (Q^2 and Q^3 units, corresponding to the final and average groups in phosphate linear chains, respectively) [41].

It is worth observing that the most significant changes of the phosphate species only occur after the treatment at 150°C . The first notable aspect of the ^{31}P NMR spectra of the thermally reduced samples is the difference in the signal-to-noise ratio of the spectrum of the GOT91_150 sample compared to the GOT11_150 and GOT12_150 samples, which is due to the much larger P content of these two latter samples, as indicated by the XRF results (Table 1). Therefore, it is possible to note the similarity between the profiles of the ^{31}P NMR spectra of these samples (GOT11_150 and GOT12_150), exhibiting a main peak around -3.0 ppm, associated with orthophosphoric acid. It is interesting to note the tendency of a slight shift of the peaks closer to 0 ppm to lower chemical shifts with increasing thermal treatment temperature, which can be attributed once more to the increase in the effects associated with the electrical conductivity and the diamagnetic susceptibility of the graphene layers in these samples, as already reported in studies involving chemically activated carbons [41].

Figure 5 shows the FTIR spectra of the prepared GOs and rGOs. The GO samples synthesized with different proportions of $\text{H}_2\text{SO}_4/\text{H}_3\text{PO}_4$ (GOT91, GOT11 and GOT12) exhibit all typical GO vibration bands around 1050 , 1618 and 1720 cm^{-1} commonly related to the stretching vibrations of C-O, C=C and C=O (of carboxylic acids) bonds, respectively. A broad band can also be observed at $\sim 3200\text{ cm}^{-1}$, associated with the stretching vibrations of -OH groups. According to previous studies on sulfur species in the chemical structure of GO [28,42,43], bands near 1215 and 1416 cm^{-1} , such as the ones observed in the spectra of the samples of the GOT91 group, can be related to S=O stretching vibrations of sulfates. The same set of bands can be observed in the spectra of the samples of the GOT11 group (at 1225 and 1390 cm^{-1}) but, knowing the considerable phosphate content of these samples (as verified by XRF and ^{31}P NMR), these bands can be related to P=O stretching vibration as well [44,45].

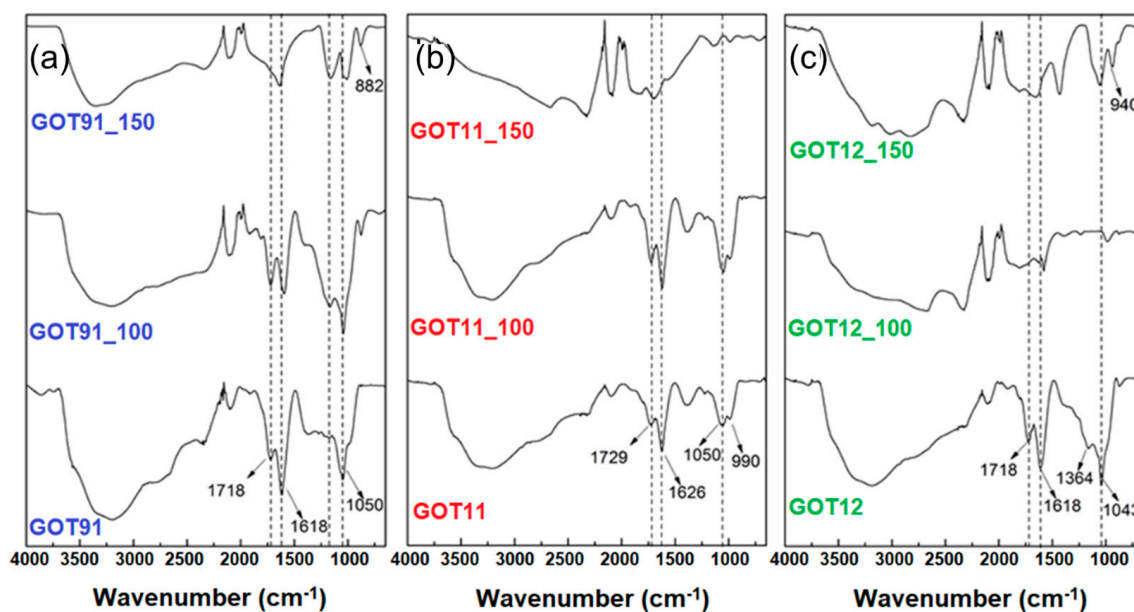


Figure 5. FTIR spectra of the (a) GOT91, (b) GOT11 and (c) GOT12 samples as prepared and after the thermal reduction treatments performed at 100 and 150 °C.

Phosphate groups are known to assemble into a polymeric arrangement and this network is dominated by linkages between PO_4 tetrahedra. As discussed previously, ^{31}P NMR results suggest that most phosphates are present in GO samples in the form of Q^0 and Q^1 units (or orthophosphoric and pyrophosphoric acids, respectively). After the thermal treatment of the GO samples at 150 °C, the ^{31}P NMR results suggested that there was a rearrangement of the phosphate groups into H_3PO_4 clusters (Q^0 units), probably interacting with the water molecules present in the GO structure [25]. In FTIR spectra, vibration bands of Q^0 and Q^1 units often appear around 890–990 cm^{-1} and 1080–1100 cm^{-1} , respectively [19,20,46]. As shown in Figure 5, it is possible to observe bands in these ranges in the FTIR spectra of GO and rGO samples (with different sulfur and phosphorus contents), mainly at 990 cm^{-1} , which is associated with H_3PO_4 molecules (Q^0 units). The band associated with Q^1 units is likely to be overlapped by the C-O vibration band at 1050 cm^{-1} of GO. However, after treatment at 150 °C, a band at this range can still be observed in the spectra of the rGO samples, suggesting the presence of ortho- and pyrophosphoric acids, in good agreement with the ^{31}P NMR results. In addition, after thermal treatment at 150 °C, broad bands around 2300 and 3000 cm^{-1} are observed, associated with vibrations of the -OH group in P-OH bonds. The stretching vibration of these P-OH bonds was previously associated with bands at 2430 and 2870 cm^{-1} and bending modes at 766 and 1256 cm^{-1} [47]. Water stretching vibrations were found at 3050 and 3350 cm^{-1} [21]. These bands were similarly observed in the spectra recorded for the samples investigated here. It is also interesting to note that even after GO thermal reduction the band related to water stretching vibrations can still be observed, which suggests the presence of adsorbed water molecules closely interacting with orthophosphoric acid.

Finally, selected P/S-rGO paper samples (prepared at 150 °C) had their electrochemical behavior evaluated. Electrodes containing the selected samples were built as shown in Figure 1. Aiming to evaluate the influence of phosphorus-containing groups on the electrochemical behavior of the studied samples, the electrochemical analyses were also conducted using an rGO sample (treated at 150 °C) prepared from a GO sample that had been synthesized by a modified Hummers method. This latter sample, labeled as GOH_150, was prepared in the same way as the other rGO samples, but without the addition of phosphoric acid during the synthesis (see Supplementary Information).

Figure 6 shows the cyclic voltammograms of the P/S-rGO and GOH_150 samples obtained at 10 mV s^{-1} (Figure 6a) and 50 mV s^{-1} (Figure 6b). All samples exhibited a

quasi-rectangular shape voltammogram, even at a high scan rate, demonstrating a good capacitive behavior of the samples. In addition, a very good electrochemical stability of the electrolyte at high potentials was observed, with no current increment related to oxygen evolution being observed even up to 1 V. The P/S-rGO samples showed higher current densities than the GOH_150 sample, which points to a higher C_s for the phosphorous-containing samples. In the voltammograms obtained at low scan rate (Figure 6a), it can be seen that the P/S-rGO hybrid samples exhibited a broad peak between 0.1 and 0.4 V, suggesting a pseudocapacitive contribution reaction that could be linked to the oxygenated and/or phosphorus-rich surface functional groups present in these samples [17].

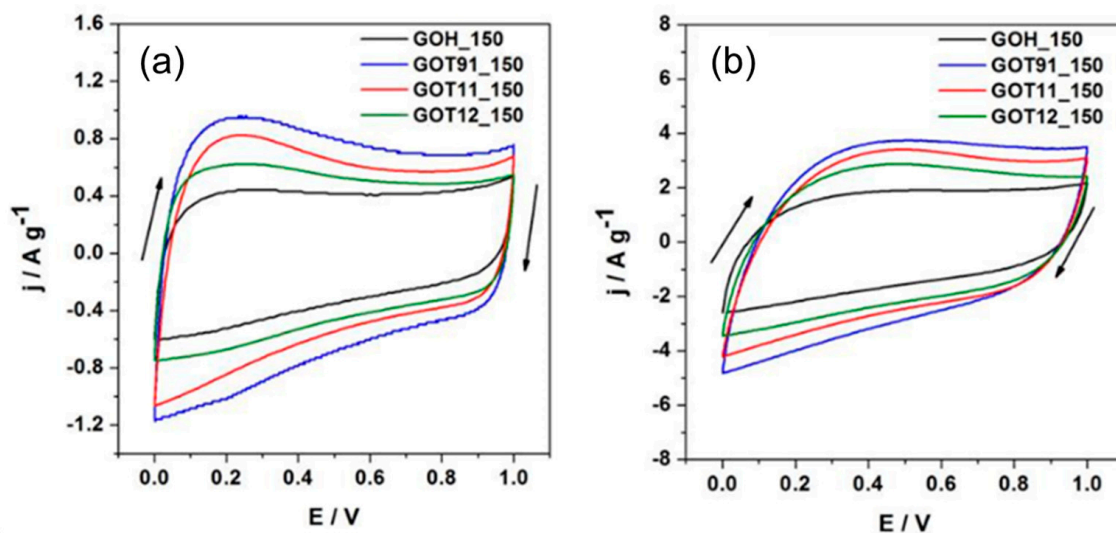


Figure 6. Cyclic voltammograms recorded at (a) 10 mV s^{-1} and (b) 50 mV s^{-1} .

The C_s values were determined from the galvanostatic charge–discharge curves according to Equation (1); their dependence on the current density is shown in Figure 7a. For all current density ranges, the P/S-rGO samples presented higher C_s values than the GOH_150 sample. The best behavior was obtained for the GOT91_150 sample, which reached values up to 155 and 110 F g^{-1} at 1 and 8 A g^{-1} , respectively. These values are similar to those reported in the literature for other carbon-based materials [48–51].

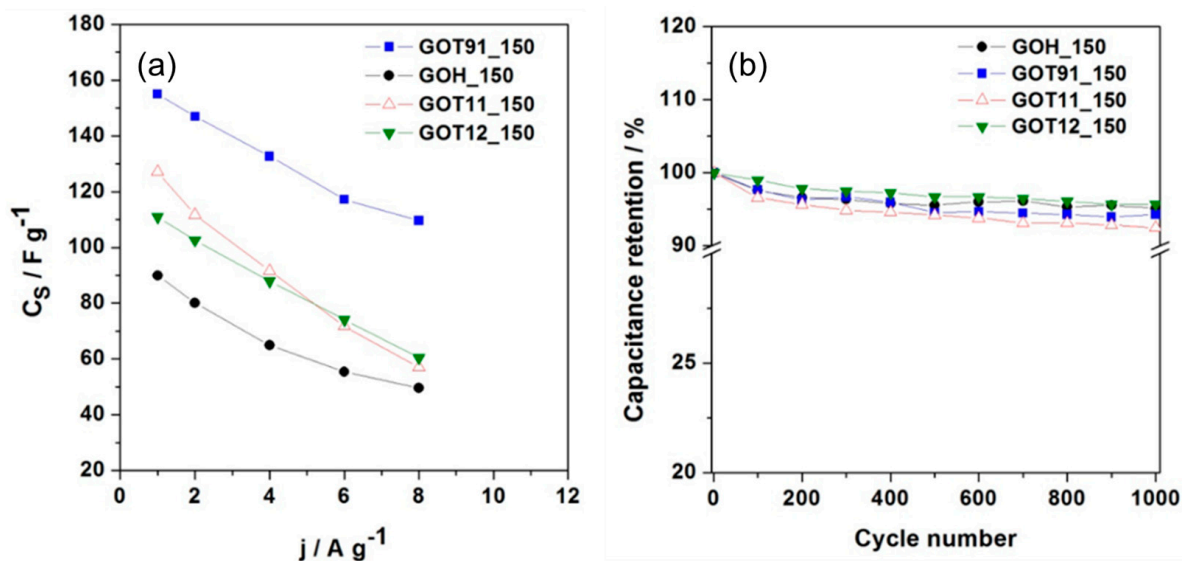


Figure 7. (a) Specific capacitance (C_s) vs. gravimetric current density (j); (b) Cyclic performance performed at 4 A g^{-1} during 1000 charge–discharge cycles.

Taking into account that the specific surface area values (see Table S3, Supplementary Information) of the rGO samples are small (less than $20 \text{ m}^2 \text{ g}^{-1}$), the analyzed samples show a significant capacitance per unit of surface area. This value is above ca. 5 F m^{-2} for the GOT91_150 sample, which is substantially higher than the values generally reported for carbon materials ($0.1\text{--}0.2 \text{ F m}^{-2}$) [50]. These results suggest the occurrence of a high pseudocapacitive contribution through the oxygenated and/or phosphorus-rich surface functional groups. Regarding this, it is observed that, on the one hand, the samples simultaneously containing phosphorus and sulfur (P/S-rGO samples) show a higher C_s value when compared to the sample not containing phosphorus (GOH_150). On the other hand, among the P/S-rGO samples, the sample with lower phosphorus content (GOT91_150) shows the highest C_s value. Therefore, the highest C_s value determined for the GOT91_150 sample could be explained by the simultaneous presence of sulfur and phosphorus functional groups linked to the pseudocapacitive phenomena, as observed in previous works on S and P co-doped porous carbons [52,53]. Still regarding the analysis of the C_s vs. j plot (Figure 7a), the GOT91_150 sample presents the best rate capability at 8 A g^{-1} (70% with respect to the C_s determined at 1 A g^{-1}), whereas the lowest rate capability (45%) is found for the GOT11_150 sample. These findings can be explained in terms of the differences in the equivalent series resistance (ESR) values of these samples (see Figure S7, in the Supplementary Information), as detailed below. Long-term charge–discharge cycling tests were performed at 4 A g^{-1} within the potential range of 0–1.0 V. The capacitance retention was calculated from the C_s value determined for each cycle divided by the C_s value of the first cycle. Figure 7b shows the capacitance retention as function of the cycle number for each sample. All the rGO samples showed good capacitance retention ($\approx 95\%$) after 1000 cycles. This demonstrates a low degradation of the samples after successive charge–discharge cycles.

The Nyquist plots of the rGO samples obtained from the EIS measurements are shown in Figure 8. It is possible to observe that all samples show a typical spectrum of a non-ideal electrochemical capacitor, with straight lines with a nearly 45° phase angle at high frequencies and more vertical lines at the low-frequency portions of the diagrams [54]. At low frequencies, the GOT11_150 sample shows the most vertical curve, suggesting a better capacitive behavior [55]. From the intercept of the curve with the real axis at high frequency, it is possible to determine the series resistance (R_s), which includes the electrolyte solution resistance, separator resistance and electrode resistance [54]. Sample GOT11_150 shows the lowest R_s value (ca. 1Ω), which indicates its good electrical conductivity. On the other hand, the GOH_150 sample shows the lowest charge transfer resistance (R_{ct}), which is associated with the diameter of the semi-circle at high frequency [55]. The sum of $R_s + R_{ct}$ is in agreement with the values of ESR determined from the galvanostatic measurements (see Figure S7, in the Supplementary Information section), with the GOT11_150 sample having the highest $R_s + R_{ct}$ value and the GOH_150 sample having the lowest one. Taking into account that, in general, a higher content of oxygenated functional groups can determine a drop in the electrical conductivity of carbon materials [51,54,56], these EIS results suggest a higher content of oxygenated functionalities in the rGO samples obtained by the modified Marcano–Tour method [22] than in the reduced sample obtained by the modified Hummers method [23].

The specific energy density (W_s) and the specific power density (P_s) were calculated considering the total mass of the two electrodes in the supercapacitor, as follows:

$$W_s (\text{Wh} \cdot \text{kg}^{-1}) = \frac{C_s \cdot E_2^2}{28.8}, \quad (2)$$

$$P_s (\text{W} \cdot \text{kg}^{-1}) = \frac{W_s}{t_d}. \quad (3)$$

In these expressions, C_s is the specific capacitance of one electrode (F g^{-1}), E_2 is the voltage range during the galvanostatic discharge (V), and t_d is the discharge time (s). Figure 9 shows the Ragone plots obtained for the rGO samples. At low P_s values, the

highest W_s value was achieved for the GOT91_150 sample (4.9 Wh kg^{-1} at 238.7 W), while the lowest one corresponded to the GOH_150 sample, which is in accordance with the C_s values obtained for these samples (i.e., the sample with the higher C_s reached the higher W_s value). On the other hand, for all the samples, as P_s increases, the W_s values decrease. This behavior is particularly noticeable for the GOT11_150 sample, which is consistent with its higher ESR (Figure S7, Supplementary Material) and relatively low rate capability (Figure 8a).

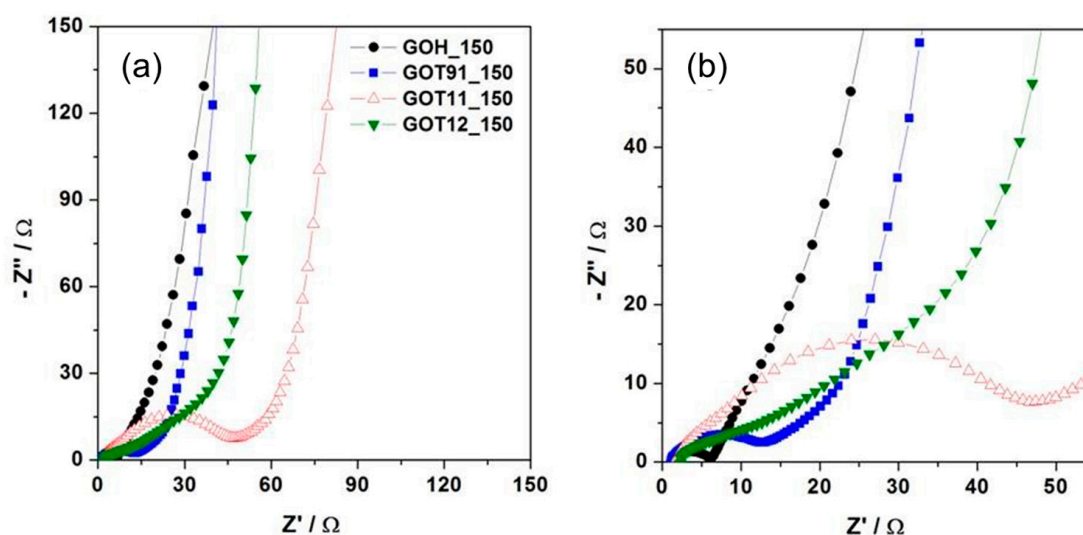


Figure 8. (a) Nyquist plots obtained for the rGO samples. (b) Zoom of a selected area of the plots exhibited in (a).

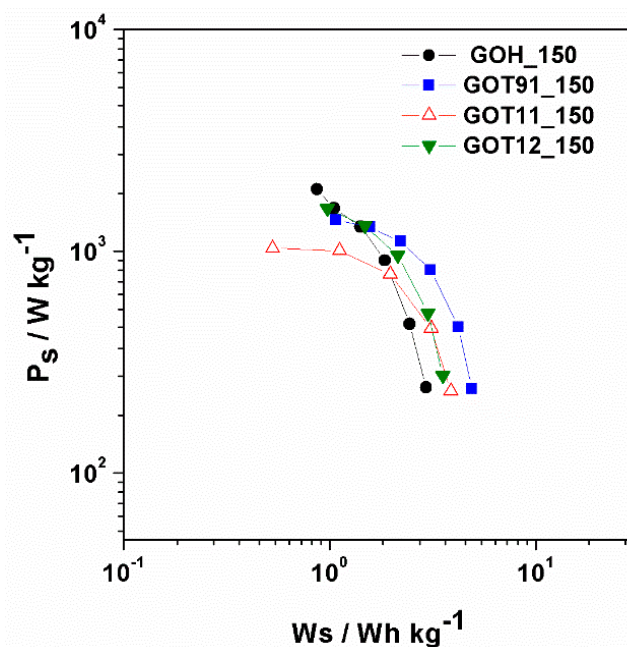


Figure 9. Specific power vs. specific energy of the electrochemical analyzed samples.

It is interesting to note that the GOH_150 sample exhibited a particularly high P_s value for the lowest W_s value (0.9 Wh kg^{-1} at 1902.5 W). If we take into account the C_s values determined at higher currents (i.e., high power), this may seem inconsistent at first, since this sample does not have a high C_s value among the rGO samples analyzed here. However, its lower ESR enables a higher voltage range (E_2) during the charge–discharge experiment (see Figure S7 in the Supplementary Information section), which results in

a higher energy accumulation. In sum, on the basis of these results, it can be concluded that the energy and power values of the supercapacitors developed from the synthesized materials are still low compared to what has been reported for other carbon materials [54]. It is clear, though, that the simultaneous presence of P- and S-containing groups in the rGO samples prepared by the simple route described here is beneficial for the promising electrochemical properties of these materials (such as good electrochemical stability in wide voltage windows, high capacitance per unit of surface area and low degradation after successive charge–discharge cycles), which stimulates the pursuit of further investigations aiming to improve the energy- and power-related properties for possible applications of these materials as supercapacitor electrodes.

4. Conclusions

By modifying the $\text{H}_2\text{SO}_4/\text{H}_3\text{PO}_4$ ratio used on the GO synthesis by the Marcano–Tour method [22], it was possible to synthesize graphene oxide samples with good degree of oxidation and varied phosphorus and sulfur contents. The thermal treatment of the P/S-GO samples at 150 °C led to the production of P/S-rGO samples containing 0.3–5 wt.% of phosphorus and 2–7 wt.% of sulfur depending on the synthesis conditions. These species were found to be present mostly as phosphate and sulfate groups, as evidenced by solid-state NMR and FTIR results. The P/S-rGO samples obtained at 150 °C had their electrochemical characteristics evaluated, and sample GOT91_150 (containing both phosphorus and sulfur) exhibited the best capacitance behavior, reaching a maximum C_s value of 155 F g^{-1} at 1 A g^{-1} , with a good rate capability at higher current density and good capacitance retention after 1000 charge–discharge cycles. Altogether, these results suggest that the simultaneous presence of sulfur and phosphorus plays a fundamental role in enhancing the capacitive properties of reduced graphene oxide samples. Even though there is still room for improvement of these features, especially regarding the energy- and power-related properties of the supercapacitors prepared from these materials, the presented methods represent a facile and low-cost alternative for the production of P/S-enriched rGO papers with promising properties (such as good electrochemical stability in wide voltage windows, high capacitance per unit of surface area and low degradation after successive charge–discharge cycles) for use in electrochemical energy-storage devices.

Supplementary Materials: The following supporting information can be downloaded at: <https://www.mdpi.com/article/10.3390/c9020060/s1>, Figure S1. X-ray diffractogram of the GOH sample after thermal treatment at 80 °C for 24 h (protocol C), compared to the XRD pattern of the graphite precursor (BG). Figure S2. X-ray diffractograms of the GOH sample after thermal treatments at various temperatures and times, according to the protocols described in Table S1. Figure S3. TG curve of the GOH sample. The dotted lines indicate the temperatures used in the thermal treatment protocols described in Table S1. The TG experiments were conducted in a Shimadzu TGA-50H instrument, using alumina pan at a heating rate of 5 °C/min, under O_2 flow (50 mL/min). Figure S4. ^{13}C NMR spectra of the GOH sample and of the rGO samples D24 and E24, which were prepared by thermally treating GOH aliquots at 100 and 150 °C, respectively, for 24 h. Figure S5. FTIR spectra of the GOH sample and of the rGO samples D24 and E24, which were prepared by thermally treating GOH aliquots at 100 and 150 °C, respectively, for 24 h. Figure S6. SEM images of GO samples and rGO papers prepared at 150 °C. Figure S7. Galvanostatic charge-discharge curves of the rGO samples obtained at a constant current density of (a) 1 A g^{-1} and (b) 8 A g^{-1} . Table S1. Description of the thermal reduction protocols used to obtain rGO from the GOH sample. Table S2. S contents of the GO sample synthesized by the modified Hummers method and the corresponding reduced materials. Table S3. Specific surface area of the rGO samples, determined from N_2 adsorption isotherms at 77 K. Refs. [57–73] are cited in the supplementary material.

Author Contributions: Conceptualization, M.A.V. and J.C.C.F.; methodology, M.A.V. and T.L.G.C.; formal analysis, M.A.V., T.L.G.C., G.R.G., D.F.C. and E.L.d.S.; data curation, M.A.V., J.C.C.F., A.C. and M.A.S.J.; writing—original draft preparation, M.A.V.; writing—review and editing, M.A.V., T.L.G.C., J.C.C.F. and E.L.d.S.; visualization, M.A.V., T.L.G.C., J.C.C.F., E.L.d.S. and A.C.; supervision, J.C.C.F.

and A.C.; project administration, J.C.C.F.; funding acquisition, J.C.C.F. and A.C. All authors have read and agreed to the published version of the manuscript.

Funding: This research was financed in part by the Coordenação de Aperfeiçoamento de Pessoal de Nível Superior—Brasil (CAPES)—Finance Code 001. The authors acknowledge also the support from the Brazilian agencies FAPES (grants 280/2021, 495/2021 and 418/2022) and CNPq (grant 310528/2022-4).

Data Availability Statement: Data sharing not applicable. No new data were created or analyzed in this study. Data sharing is not applicable to this article.

Acknowledgments: Laboratory for Research and Development of Methodologies for Crude Oil Analysis (LabPetro), Laboratory of Thermal Plasma (LPT), Laboratory of Air Quality, located at the Federal University of Espírito Santo (UFES), Brazil, for the use of their experimental facilities. The support from the Comisión Académica de Posgrado (CAP), Universidad de la República, Uruguay, is also gratefully acknowledged.

Conflicts of Interest: The authors declare no conflict of interest.

References

1. Novoselov, K.S.; Geim, A.K.; Morozov, S.V.; Jiang, D.; Zhang, Y.; Dubonos, S.V.; Grigorieva, I.V.; Firsov, A.A. Electric Field Effect in Atomically Thin Carbon Films. *Science* **2004**, *306*, 666–669. [[CrossRef](#)] [[PubMed](#)]
2. Brodie, B.C. On the Atomic Weight of Graphite. *Philos. Trans. R. Soc. Lond.* **1859**, *149*, 249–259.
3. Pei, S.; Cheng, H.M. The Reduction of Graphene Oxide. *Carbon* **2012**, *50*, 3210–3228. [[CrossRef](#)]
4. Huang, H.; Shi, H.; Das, P.; Qin, J.; Li, Y.; Wang, X.; Su, F.; Wen, P.; Li, S.; Lu, P.; et al. The Chemistry and Promising Applications of Graphene and Porous Graphene Materials. *Adv. Funct. Mater.* **2020**, *30*, 1909035. [[CrossRef](#)]
5. Dreyer, D.R.; Park, S.; Bielawski, C.W.; Ruoff, R.S. The chemistry of graphene oxide. *Chem. Soc. Rev.* **2009**, *39*, 228–240. [[CrossRef](#)] [[PubMed](#)]
6. Brisebois, P.P.; Sijaj, M. Harvesting Graphene Oxide—Years 1859 to 2019: A Review of Its Structure, Synthesis, Properties and Exfoliation. *J. Mater. Chem. C* **2020**, *8*, 1517–1547. [[CrossRef](#)]
7. Park, S.; An, J.; Potts, J.R.; Velamakanni, A.; Murali, S.; Ruoff, R.S. Hydrazine-Reduction of Graphite-and Graphene Oxide. *Carbon* **2011**, *49*, 3019–3023. [[CrossRef](#)]
8. De Silva, K.K.H.; Huang, H.H.; Joshi, R.K.; Yoshimura, M. Chemical Reduction of Graphene Oxide Using Green Reductants. *Carbon* **2017**, *119*, 190–199. [[CrossRef](#)]
9. Zhou, Q.; Zhao, Z.; Chen, Y.; Hu, H.; Qiu, J. Low Temperature Plasma-Mediated Synthesis of Graphene Nanosheets for Supercapacitor Electrodes. *J. Mater. Chem.* **2012**, *22*, 6061–6066. [[CrossRef](#)]
10. Ghadim, E.E.; Rashidi, N.; Kimiagar, S.; Akhavan, O.; Manouchehri, F.; Ghaderi, E. Pulsed Laser Irradiation for Environment Friendly Reduction of Graphene Oxide Suspensions. *Appl. Surf. Sci.* **2014**, *301*, 183–188. [[CrossRef](#)]
11. Dumée, L.F.; Feng, C.; He, L.; Allieux, F.M.; Yi, Z.; Gao, W.; Banos, C.; Davies, J.B.; Kong, L. Tuning the Grade of Graphene: Gamma Ray Irradiation of Free-Standing Graphene Oxide Films in Gaseous Phase. *Appl. Surf. Sci.* **2014**, *322*, 126–135. [[CrossRef](#)]
12. Okhay, O.; Gonçalves, G.; Tkach, A.; Dias, C.; Ventura, J.; Ribeiro Da Silva, M.F.; Valente Gonçalves, L.M.; Titus, E. Thin Film versus Paper-like Reduced Graphene Oxide: Comparative Study of Structural, Electrical, and Thermoelectrical Properties. *J. Appl. Phys.* **2016**, *120*, 051706. [[CrossRef](#)]
13. Khan, F.; Khan, S.; Kamal, S.; Arshad, M. Recent Advances in Graphene Oxide and Reduced Graphene Oxide Based Nanocomposites for the Photodegradation of Dyes. *J. Mater. Chem. C* **2020**, *8*, 15940–15955. [[CrossRef](#)]
14. Zhu, Y.; Murali, S.; Cai, W.; Li, X.; Suk, J.W.; Potts, J.R.; Ruoff, R.S. Graphene and Graphene Oxide: Synthesis, Properties, and Applications. *Adv. Mater.* **2010**, *22*, 3906–3924. [[CrossRef](#)]
15. Valentini, C.; Montes-Garcia, V.; Livio, P.A.; Chudziak, T.; Raya, J.; Ciesielski, A.; Samorì, P. Tuning the electrical properties of graphene oxide through low-temperature thermal annealing. *Nanoscale* **2023**, *15*, 5743–5755. [[CrossRef](#)] [[PubMed](#)]
16. Kumar, N.A.; Baek, J. Doped Graphene Supercapacitors. *Nanotechnology* **2015**, *26*, 492001. [[CrossRef](#)]
17. Yu, X.; Feng, L.; Park, H.S. Highly Flexible Pseudocapacitors of Phosphorus-Incorporated Porous Reduced Graphene Oxide Films. *J. Power Sources* **2018**, *390*, 93–99. [[CrossRef](#)]
18. Qiao, X.; Liao, S.; You, C.; Chen, R. Phosphorus and Nitrogen Dual Doped and Simultaneously Reduced Graphene Oxide with High Surface Area as Efficient Metal-Free Electrocatalyst for Oxygen Reduction. *Catalysts* **2015**, *5*, 981–991. [[CrossRef](#)]
19. Ghafari, H.; Talebi, M. Water-Soluble Phosphated Graphene: Preparation, Characterization, Catalytic Reactivity, and Adsorption Property. *Ind. Eng. Chem. Res.* **2016**, *55*, 2970–2982. [[CrossRef](#)]
20. Niu, F.; Tao, L.-M.; Deng, Y.-C.; Wang, Q.-H.; Song, W.-G. Phosphorus Doped Graphene Nanosheets for Room Temperature NH₃ Sensing. *N. J. Chem.* **2014**, *38*, 2269. [[CrossRef](#)]
21. Sun, X.; Cheng, P.; Wang, H.; Xu, H.; Dang, L.; Liu, Z.; Lei, Z. Activation of Graphene Aerogel with Phosphoric Acid for Enhanced Electrocapacitive Performance. *Carbon* **2015**, *92*, 1–10. [[CrossRef](#)]

22. Marcano, D.C.; Kosynkin, D.V.; Berlin, J.M.; Sinititskii, A.; Sun, Z.; Slesarev, A.; Alemany, L.B.; Lu, W.; Tour, J.M. Improved Synthesis of Graphene Oxide. *ACS Nano* **2010**, *4*, 4806–4814. [[CrossRef](#)] [[PubMed](#)]
23. Hummers, W.S.; Offeman, R.E. Preparation of Graphitic Oxide. *J. Am. Chem. Soc.* **1958**, *80*, 1339. [[CrossRef](#)]
24. Chua, C.K.; Sofer, Z.; Pumera, M. Graphite Oxides: Effects of Permanganate and Chlorate Oxidants on the Oxygen Composition. *Chem.-A Eur. J.* **2012**, *18*, 13453–13459. [[CrossRef](#)] [[PubMed](#)]
25. Costa, T.L.G.; Vieira, M.A.; Gonçalves, G.R.; Cipriano, D.F.; Lacerda Jr., V.; Gonçalves, A.S.; Scopel, W.L.; de Siervo, A.; Freitas, J.C.C. Combined computational and experimental study about the incorporation of phosphorus into the structure of graphene oxide. *Phys. Chem. Chem. Phys.* **2023**, *25*, 6927–6943. [[CrossRef](#)]
26. Cory, D.G.; Ritchey, W.M. Suppression of Signals from the Probe in Bloch Decay Spectra. *J. Magn. Reson.* **1988**, *32*, 128–132. [[CrossRef](#)]
27. Sanderson, K. Carbon Makes Super-Tough Paper. *Nature* **2007**. [[CrossRef](#)]
28. Eigler, S.; Dotzer, C.; Hof, F.; Bauer, W.; Hirsch, A. Sulfur Species in Graphene Oxide. *Chem.-A Eur. J.* **2013**, *19*, 9490–9496. [[CrossRef](#)]
29. Farjadian, F.; Abbaspour, S.; Sadatlu, M.A.A.; Mirkiani, S.; Ghasemi, A.; Hoseini-Ghahfarokhi, M.; Mozaffari, N.; Karimi, M.; Hamblin, M.R. Recent Developments in Graphene and Graphene Oxide: Properties, Synthesis, and Modifications: A Review. *ChemistrySelect* **2020**, *5*, 10200–10219. [[CrossRef](#)]
30. Moreno-Fernández, G.; Gomes-Urbano, J.L.; Enterria, M.; Cid, R.; López del Amo, J.M.; Mysyk, R.; Carriazo, D. Understanding enhanced charge storage of phosphorus-functionalized graphene in aqueous acidic electrolytes. *Electrochim. Acta* **2020**, *361*, 136985. [[CrossRef](#)]
31. Dreyer, D.R.; Todd, A.D.; Bielawski, C.W. Harnessing the Chemistry of Graphene Oxide. *Chem. Soc. Rev.* **2014**, *43*, 5288–5301. [[CrossRef](#)]
32. Aliyev, E.; Filiz, V.; Khan, M.M.; Lee, Y.J.; Abetz, C.; Abetz, V. Structural Characterization of Graphene Oxide: Surface Functional Groups and Fractionated Oxidative Debris. *Nanomaterials* **2019**, *9*, 1180. [[CrossRef](#)]
33. Skákalová, V.; Kotrusz, P.; Jergel, M.; Susi, T.; Mittelberger, A.; Vretenár, V.; Šiffalovič, P.; Kotakoski, J.; Meyer, J.C.; Hulman, M. Chemical Oxidation of Graphite: Evolution of the Structure and Properties. *J. Phys. Chem. C* **2018**, *122*, 929–935. [[CrossRef](#)]
34. Gao, W.; Alemany, L.B.; Ci, L.; Ajayan, P.M. New Insights into the Structure and Reduction of Graphite Oxide. *Nat. Chem.* **2009**, *1*, 403–408. [[CrossRef](#)] [[PubMed](#)]
35. He, H.; Riedl, T.; Lerf, A.; Klinowski, J. Solid-State NMR Studies of the Structure of Graphite Oxide. *J. Phys. Chem.* **1996**, *100*, 19954–19958. [[CrossRef](#)]
36. Rawal, A.; Man, S.H.C.; Agarwal, V.; Yao, Y.; Thickett, S.C.; Zetterlund, P.B. Structural Complexity of Graphene Oxide: The Kirigami Model. *ACS Appl. Mater. Interfaces* **2021**, *13*, 18255–18263. [[CrossRef](#)]
37. Freitas, J.C.C.; Emmerich, F.G.; Cernicchiaro, G.R.C.; Sampaio, L.C.; Bonagamba, T.J. Magnetic Susceptibility Effects on ¹³C MAS NMR Spectra of Carbon Materials and Graphite. *Solid State Nucl. Magn. Reson.* **2001**, *20*, 61–73. [[CrossRef](#)] [[PubMed](#)]
38. Vieira, M.A.; Gonçalves, G.R.; Cipriano, D.F.; Schettino, M.A.; Silva Filho, E.A.; Cunha, A.G.; Emmerich, F.G.; Freitas, J.C.C. Synthesis of Graphite Oxide from Milled Graphite Studied by Solid-State ¹³C Nuclear Magnetic Resonance. *Carbon* **2016**, *98*, 496–503. [[CrossRef](#)]
39. Puziy, A.M.; Poddubnaya, O.I.; Socha, R.P.; Gurgul, J.; Wisniewski, M. XPS and NMR Studies of Phosphoric Acid Activated Carbons. *Carbon* **2008**, *46*, 2113–2123. [[CrossRef](#)]
40. Wang, Y.; Zuo, S.; Yang, J.; Yoon, S.H. Evolution of Phosphorus-Containing Groups on Activated Carbons during Heat Treatment. *Langmuir* **2017**, *33*, 3112–3122. [[CrossRef](#)] [[PubMed](#)]
41. Lopes, T.R.; Cipriano, D.F.; Gonçalves, G.R.; Honorato, H.A.; Schettino, M.A.; Cunha, A.G.; Emmerich, F.G.; Freitas, J.C.C. Multinuclear Magnetic Resonance Study on the Occurrence of Phosphorus in Activated Carbons Prepared by Chemical Activation of Lignocellulosic Residues from the Babassu Production. *J. Environ. Chem. Eng.* **2017**, *5*, 6016–6029. [[CrossRef](#)]
42. Zhou, Y.; Ma, R.; Candelaria, S.L.; Wang, J.; Liu, Q.; Uchaker, E.; Li, P.; Chen, Y.; Cao, G. Phosphorus/Sulfur Co-Doped Porous Carbon with Enhanced Specific Capacitance for Supercapacitor and Improved Catalytic Activity for Oxygen Reduction Reaction. *J. Power Sources* **2016**, *314*, 39–48. [[CrossRef](#)]
43. Yu, X.; Kang, Y.; Park, H.S. Sulfur and Phosphorus Co-Doping of Hierarchically Porous Graphene Aerogels for Enhancing Supercapacitor Performance. *Carbon* **2016**, *101*, 49–56. [[CrossRef](#)]
44. Ying, K.; Tian, R.; Zhou, J.; Li, H.; Dugnani, R.; Lu, Y.; Duan, H.; Guo, Y.; Liu, H. A Three Dimensional Sulfur/Reduced Graphene Oxide with Embedded Carbon Nanotubes Composite as a Binder-Free, Free-Standing Cathode for Lithium-Sulfur Batteries. *RSC Adv.* **2017**, *7*, 43483–43490. [[CrossRef](#)]
45. Thomas, H.R.; Marsden, A.J.; Walker, M.; Wilson, N.R.; Rourke, J.P. Sulfur-Functionalized Graphene Oxide by Epoxide Ring-Opening. *Angew. Chem. Int. Ed.* **2014**, *53*, 7613–7618. [[CrossRef](#)]
46. Bi, Z.; Huo, L.; Kong, Q.; Li, F.; Chen, J.; Ahmad, A.; Wei, X.; Xie, L.; Chen, C. Structural Evolution of Phosphorus Species on Graphene with a Stabilized Electrochemical Interface. *Appl. Mater. Interfaces* **2019**, *11*, 11421–11430. [[CrossRef](#)]
47. Al, M.; Oh, P.O.; Frost, R.L.; Scholz, R.; López, A.; Xi, Y. A Vibrational Spectroscopic Study of the Phosphate Mineral Whiteite CaMn⁽⁺⁺⁾Mg₂Al₂(PO₄)₄(OH)₂·8(H₂O). *Spectrochim. Acta Part A Mol. Biomol. Spectrosc.* **2014**, *124*, 243–248.
48. Gurusamy, L.; Anandan, S.; Liu, N.; Wu, J.J. Synthesis of a Novel Hybrid Anode Nanoarchitecture of Bi₂O₃/Porous-RGO Nanosheets for High-Performance Asymmetric Supercapacitor. *J. Electroanal. Chem.* **2020**, *856*, 113489. [[CrossRef](#)]

49. Zhao, X.; Li, W.; Kong, F.; Chen, H.; Wang, Z.; Liu, S.; Jin, C. Carbon Spheres Derived from Biomass Residue via Ultrasonic Spray Pyrolysis for Supercapacitors. *Mater. Chem. Phys.* **2018**, *219*, 461–467. [[CrossRef](#)]
50. Pandolfo, A.G.; Hollenkamp, A.F. Carbon Properties and Their Role in Supercapacitors. *J. Power Sources* **2006**, *157*, 11–27. [[CrossRef](#)]
51. Cuña, A.; Ortega Vega, M.R.; da Silva, E.L.; Tancredi, N.; Radtke, C.; Malfatti, C.F. Nitric Acid Functionalization of Carbon Monoliths for Supercapacitors: Effect on the Electrochemical Properties. *Int. J. Hydrogen Energy* **2016**, *41*, 12127–12135. [[CrossRef](#)]
52. Liu, Y.; Chang, Z.; Yao, L.; Yan, S.; Lin, J.; Chen, J.; Lian, J.; Lin, H. Nitrogen/Sulfur Dual-Doped Sponge-like Porous Carbon Materials Derived from Pomelo Peel Synthesized at Comparatively Low Temperatures for Superior-Performance Supercapacitors. *J. Electroanal. Chem.* **2019**, *847*, 113111. [[CrossRef](#)]
53. Qiang, Z.; Dan, D.; Wang, M.; Xiong, C.; Ying, X.; Jie, Z. Sulfur Modification of Carbon Materials as Well as the Redox Additive of Na₂S for Largely Improving Capacitive Performance of Supercapacitors. *J. Electroanal. Chem.* **2020**, *856*, 113678.
54. Béguin, F.; Frackowiak, E. *Supercapacitors: Materials, Systems, and Applications*; Wiley-VCH: Hoboken, NJ, USA, 2013.
55. Mishra, A.K.; Ramaprabhu, S. Functionalized Graphene-Based Nanocomposites for Supercapacitor Application. *J. Phys. Chem. C* **2011**, *115*, 14006–14013. [[CrossRef](#)]
56. Cuña, A.; Tancredi, N.; Bussi, J.; Deiana, A.C.; Sardella, M.F.; Barranco, V.; Rojo, J.M.E. Grandis as a Biocarbons Precursor for Supercapacitor Electrode Application. *Waste Biomass Valorization* **2014**, *5*, 305–313. [[CrossRef](#)]
57. Vieira, M.A.; Frasson, C.M.R.; Costa, T.L.G.; Cipriano, D.F.; Schettino, M.A.; Cunha, A.G.; Freitas, J.C.C. Solid state ¹³C NMR study on the synthesis of graphite oxide from different graphitic precursors. *Quim. Nova* **2017**, *40*, 1164–1171.
58. Jeong, H.K.; Jin, M.H.; So, K.P.; Lim, S.C.; Lee, Y.H. Tailoring the characteristics of graphite oxides by different oxidation times. *J. Phys. D Appl. Phys.* **2009**, *42*, 065418. [[CrossRef](#)]
59. Wang, H.; Hu, Y.H. Effect of oxygen content on structures of graphite oxides. *Ind. Eng. Chem. Res.* **2011**, *50*, 6132–6137. [[CrossRef](#)]
60. Mu, S.J.; Su, Y.C.; Xiao, L.H.; Liu, S.D.; Hu, T.; Tang, H.B. X-ray Diffraction Pattern of Graphite Oxide. *Chin. Phys. Lett.* **2013**, *30*, 096101. [[CrossRef](#)]
61. Rattana, T.; Chaiyakun, S.; Witit-Anun, N.; Nuntawong, N.; Chindaudom, P.; Oaew, S.; Kedkeaw, C.; Limsuwan, P. Preparation and characterization of graphene oxide nanosheets. *Procedia Eng.* **2012**, *32*, 759–764. [[CrossRef](#)]
62. Huh, S.H. *Thermal Reduction of Graphene Oxide*; Mikhailov, S., Ed.; InTech: London, UK, 2011; Volume 19, pp. 73–90.
63. Stankovich, S.; Dikin, D.A.; Piner, R.D.; Kohlhaas, K.A.; Kleinhammes, A.; Jia, Y.; Wu, Y.; Nguyen, S.T.; Ruoff, R.S. Synthesis of graphene-based nanosheets via chemical reduction of exfoliated graphite oxide. *Carbon* **2007**, *45*, 1558–1565. [[CrossRef](#)]
64. Krishnamoorthy, K.; Veerapandian, M.; Yun, K.; Kim, S.J. The chemical and structural analysis of graphene oxide with different degrees of oxidation. *Carbon* **2013**, *53*, 38–49. [[CrossRef](#)]
65. Tegou, E.; Pseiropoulos, G.; Filippidou, M.K.; Chatzandroulis, S. Low-temperature thermal reduction of graphene oxide films in ambient atmosphere: Infra-red spectroscopic studies and gas sensing applications. *Microelectron. Eng.* **2016**, *159*, 146–150. [[CrossRef](#)]
66. Hontoria-Lucas, C.; López-Peinado, A.J.; López-González, J.D.; Rojas-Cervantes, M.L.; Martín-Aranda, R.M. Study of oxygen-containing groups in a series of graphite oxides: Physical and chemical characterization. *Carbon* **1995**, *33*, 1585–1592. [[CrossRef](#)]
67. Cai, W.; Piner, R.D.; Stadermann, F.J.; Park, S.; Shaibat, M.A.; Ishii, Y.; Yang, D.; Velamakanni, A.; An, S.J.; Stoller, M.; et al. Synthesis and Solid-State NMR Structural Characterization of ¹³C-Labeled Graphite Oxide. *Science* **2008**, *321*, 1815–1817. [[CrossRef](#)] [[PubMed](#)]
68. Lerf, A.; He, H.; Forster, M.; Klinowski, J. Structure of Graphite Oxide Revisited. *J. Phys. Chem. B* **1998**, *102*, 4477–4482. [[CrossRef](#)]
69. Dimiev, A.M.; Eigler, S. *Graphene Oxide: Fundamentals and Applications*, 1st ed.; John Wiley & Sons, Ltd.: Chichester, UK, 2016.
70. Sorokina, N.E.; Shornikova, O.N.; Avdeev, V.V. Stability limits of graphite intercalation compounds in the systems graphite-HNO₃(H₂SO₄)-H₂O-KMnO₄. *Inorg. Mater.* **2007**, *43*, 822–826. [[CrossRef](#)]
71. Dimiev, A.M.; Polson, T.A. Contesting the two-component structural model of graphene oxide and reexamining the chemistry of graphene oxide in basic media. *Carbon* **2015**, *93*, 544–554. [[CrossRef](#)]
72. Brunauer, S.; Emmett, P.H.; Teller, E. Adsorption of Gases in Multimolecular Layers. *J. Am. Chem. Soc.* **1938**, *60*, 309–319. [[CrossRef](#)]
73. Ouyang, Z.; Lei, Y.; Chen, Y.; Zhang, Z.; Jiang, Z.; Hu, J. Preparation and Specific Capacitance Properties of Sulfur, Nitrogen Co-Doped Graphene Quantum Dots. *Nanoscale Res. Lett.* **2019**, *14*, 1–9. [[CrossRef](#)] [[PubMed](#)]

Disclaimer/Publisher’s Note: The statements, opinions and data contained in all publications are solely those of the individual author(s) and contributor(s) and not of MDPI and/or the editor(s). MDPI and/or the editor(s) disclaim responsibility for any injury to people or property resulting from any ideas, methods, instructions or products referred to in the content.